NeuroImage: Clinical 21 (2019) 101608

Contents lists available at ScienceDirect

NeuroImage: Clinical

journal homepage: www.elsevier.com/locate/ynicl

Fully automated tissue segmentation of the prescription isodose region delineated through the Gamma knife plan for cerebral arteriovenous malformation (AVM) using fuzzy C-means (FCM) clustering

Syu-Jyun Peng[a,b], Cheng-chia Lee[c,d], Hsiu-Mei Wu[d,e], Chung-Jung Lin[d,e], Cheng-Ying Shiau[d,f], Wan-Yuo Guo[d,e], David Hung-Chi Pan[c,d,g], Kang-Du Liu[c,d], Wen-Yuh Chung[c,d], Huai-Che Yang[c,d,*]

[a] Biomedical Electronics Translational Research Center, National Chiao Tung University, Hsinchu, Taiwan
[b] Institute of Electronics, National Chiao-Tung University, Hsinchu, Taiwan
[c] Department of Neurosurgery, Neurological Institute, Taipei Veterans General Hospital, Taipei, Taiwan
[d] School of Medicine, National Yang-Ming University, Taipei, Taiwan
[e] Department of Radiology, Taipei Veterans General Hospital, Taipei, Taiwan
[f] Cancer Center, Taipei Veterans General Hospital, Taipei, Taiwan
[g] Shuang-Ho Hospital, Taipei Medical University, Taipei, Taiwan

ARTICLE INFO

Keywords:
Cerebral Arterio-Venous Malformation
Gamma knife radiosurgery
Radiotherapy
Radiation side-effect
Fuzzy c-means clustering

ABSTRACT

Background: Gamma knife radiosurgery (GKRS) is a common treatment for cerebral arterio-venous malformations (AVMs), particularly in cases where the malformation is deep-seated, large, or in eloquent areas of the brain. Unfortunately, these procedures can result in radiation injury to brain parenchyma. The fact that every AVM is unique in its vascular morphology makes it nearly impossible to exclude brain parenchyma from isodose radiation exposure during the formulation of a GKRS plan. Calculating the percentages of the various forms of tissue exposed to specific doses of radiation is crucial to understanding the clinical responses and causes of brain parenchyma injury following GKRS for AVM.

Methods: In this study, we developed a fully automated algorithm using unsupervised classification via fuzzy c-means clustering for the analysis of T2 weighted images used in a Gamma knife plan. This algorithm is able to calculate the percentages of nidus, brain tissue, and cerebrospinal fluid (CSF) within the prescription isodose radiation exposure region.

Results: The proposed algorithm was used to assess the treatment plan of 25 patients with AVM who had undergone GKRS. The Dice similarity index (SI) was used to determine the degree of agreement between the results obtained using the algorithm and a visually guided manual method (the gold standard) performed by an experienced neurosurgeon. In the nidus, the SI was (74.86 ± 1.30%) (mean ± standard deviation), the sensitivity was (83.05 ± 11.91)%, and the specificity was (86.73 ± 10.31)%. In brain tissue, the SI was (79.50 ± 6.01)%, the sensitivity was (73.05 ± 9.77)%, and the specificity was (85.53 ± 7.13)%. In the CSF, the SI was (69.57 ± 15.26)%, the sensitivity was (89.86 ± 5.87)%, and the specificity was (92.36 ± 4.35)%.

Conclusions: The proposed clustering algorithm provides precise percentages of the various types of tissue within the prescription isodose region in the T2 weighted images used in the GKRS plan for AVM. Our results shed light on the causes of brain radiation injury after GKRS for AVM. In the future, this system could be used to improve outcomes and avoid complications associated with GKRS treatment.

1. Introduction

Cerebral arterio-venous malformation (AVM) is a congenital cerebral vascular anomaly with an incidence rate estimated at 1.12–1.34 per 100,000 person years (Al-Shahi et al., 2003). An AVM comprises an abnormal nidus of blood vessels that shunt blood directly from an artery to a vein and thereby bypass an intervening capillary bed (Joint Writing Group of the Technology Assessment Committee American Society of Interventional and Therapeutic Neuroradiology et al., 2001). The symptoms of cerebral AVM include hemorrhagic stroke, seizure, and

* Corresponding author at: Department of Neurosurgery, Neurological Institute, Taipei Veterans General Hospital, 17F, No. 201, Shih-Pai Road, Sec. 2, Beitou, Taipei 11217, Taiwan.
E-mail address: wade012@gmail.com (H.-C. Yang).

https://doi.org/10.1016/j.nicl.2018.11.018
Received 19 May 2018; Received in revised form 31 August 2018; Accepted 18 November 2018
Available online 19 November 2018

headache. These vascular lesions account for 9% of subarachnoid hemorrhages and 1–2% of all strokes (Ogilvy et al., 2001). Gamma knife radiosurgery (GKRS) is a common approach to the treatment of cerebral AVM, particularly in cases where the AVM is located at depth or in a functional area of the brain that is deemed too risky for resection. Following radiosurgery, 80% of patients show complete obliteration of the AVM in long-term follow-up (Bollet et al., 2004; Lunsford et al., 1991; Pan et al., 2000). However, it can take 2–3 years after GKRS before the AVM is obliterated, and adverse radiation effects (ARE) during the latency period can lead to brain edema (Yen et al., 2013).

The underlying causes of AREs are still unclear. Researchers have hypothesized that AREs are related to brain parenchyma injuries, which occur close to the nidus of AVM during GKRS treatment. The niduses of AVM are unique in terms of size and vascular morphology. Some present a compact vascular structure with little brain tissue, whereas others are spread out and intermingled with brain tissue. The later (diffuse type) are more likely to receive higher doses of radiation during GKRS treatment. A lack of tools for the quantitative analysis of images for the evaluation of GKRS plans means that the hypothesis of volume-dependent adverse radiation effects after GKRS cannot be proven.

In fuzzy c-means (FCM) clustering, each data point may belong to more than one cluster (Cannon et al., 1986; Hathaway and Bezdek, 2001). This image analysis technique is well established in tumor detection (Gatos et al., 2017). Clustering and cluster analysis involves assigning data points to clusters to ensure that items in a given cluster are as similar as possible and that items belonging to different clusters are as dissimilar as possible. Clusters are identified using similarity measures, such as distance, connectivity, and intensity. The choice about which measures to use is based on available data or the intended application.

Our objective in this study was to use the FCM technique to classify the prescription isodose radiation exposure range in T2 weighted (T2W) images for GKRS plans with the aim of calculating precise percentages and volumes of the various forms of tissue.

2. Methods

The algorithm proposed in this study is intended for fully automated image analysis. In brief, the dose intensity distribution of a GKRS plan is first converted into a corresponding 3D special position in a T2w image set via linear interpolation. The prescription isodose region is then identified to specify the ROI, whereupon the voxels within the ROI are classified according to intensity via FCM clustering. Finally, the volumes or ratios of the various forms of tissue within the ROI are calculated.

2.1. Subjects

Twenty five patients (age range 9.7–77.2 years) with cerebral AVM who had been admitted to Taipei Veterans General Hospital were randomly recruited for this study. Written, informed consent was obtained from each participating patient. The protocol of this research was approved and monitored by Taipei Veterans General Hospital Institutional Review Board.

GKRS plans were drawn up using the various pulse sequences of MR images (T1w, T2w, and TOF) to locate the margin of the AVM nidus. During the planning process, we delineated the margin of the nidus in the MR images and compared these results with findings obtained from angiograms. Among the various pulse sequence images used during GKRS planning, T2w images provided the best tissue resolution for differentiating among the three tissue components in gray scale.

2.2. MR imaging protocol

All MRI data of patients with cerebral AVM were collected using a Signa HDxt 1.5 T (GE healthcare Milwaukee, WI) scanner with an eight-channel phased-array neurovascular coil to obtain T2w and magnetic resonance angiography time of flight (TOF) sequences. The T2w images were used for subsequent data processing because they provided the best tissue contrast and resolution, wherein brain tissue appeared gray, the nidus appeared black (due to flow void effects), and the CSF space appeared white. The parameters used in acquiring the T2w sequences were as follows: repetition time (TR) = 4000–5500 ms, echo time (TE) = 80–100 ms, field of view (FOV) = 260 mm, number of excitations (NEX) = 2, slice thickness = 3 mm, and slice gap = 0 mm. The parameters for acquiring TOF sequence were TR = 6.9 ms, TE = 45 ms, FOV = 260 mm, NEX = 2, slice thickness = 1.5–2 mm, and slice gap = 1.5–2 mm.

2.3. Manual clustering

Manual clustering was performed by an experienced neurosurgeon (H.C. Yang) according to the radiation exposure region and T2w intensity. Preprocessing was performed to obtain the boundary of the prescription isodose region within the parenchymal brain in T2w images. The areas of the nidus, brain tissue, and CSF within the boundary were identified via manual demarcation using Paintbrush software. The neurosurgeon recognized the black and white of the T2w intensity as the nidus and CSF, respectively. The remaining voxels were regarded as brain tissue. The location of cerebral AVM was determined according to the corresponding neuroanatomy observed in the images. For example, the blue, green, and red curves in the T2w intensity histogram shown in Fig. 1 respectively illustrate the manually demarcated nidus, brain tissue, and CSF.

2.4. Automated clustering

We developed an automated (i.e., unsupervised) clustering algorithm using FCM that is capable of analyzing T2w images of the radiation exposure region of the brain that had been delineated in the GKRS plan. The algorithm was used to calculate the various percentages of nidus, brain tissue, and CSF. The program was run on a personal computer with Intel Core™ i7-6700HQ CPU@ 2.60 GHz with 16 GB RAM. The procedure was conducted primarily in the MATLAB environment (MathWorks Inc., Natick, Massachusetts). As shown in Fig. 2, analysis and automated clustering consisted of 7 steps, which required a total of 3.47 ± 1.29 s for execution for each case. The details of each step are described in the following:

Step 1. Interpolation The dose intensity distribution from the dose map is converted into corresponding spatial positions on the T2w images using linear interpolation, and the Dose Grid Scaling factor is extracted from the header information of the dose data. The dose intensity distribution at the various voxel positions in the T2w image are then multiplied by the Dose Grid Scaling factor to obtain the radiation dose intensity distribution in centigrays (cGys).

Step 2. Selection of prescription isodose region After selecting a prescribed peripheral radiation dose intensity, the selected radiation exposure region included the entire area in the T2w images that received radiation dose intensity equal to or greater than the prescription dose intensity.

Step 3. Registration The TOF is registered to the corresponding T2w image via 3-D voxel registration using the normalized mutual information method to correct for differences resulting from head movement (Maes et al., 1997).

Step 4. Brain mask extraction A brain mask is extracted from the registered TOF based on estimates of the inner and outer skull surfaces using BET (Brain Extraction Tool), a software package developed at the FMRIB Centre, University of Oxford, Oxford, United Kingdom (Smith, 2002).

Step 5. ROI definition The ROI is identified using a logical AND operation applied to the selected radiation exposure region and brain mask.

Step 6. Fuzzy c-means classification The voxels in the ROI of a T2w image are classified as the nidus, brain tissue, or CSF, according to differences in voxel intensity between the various forms of tissue.

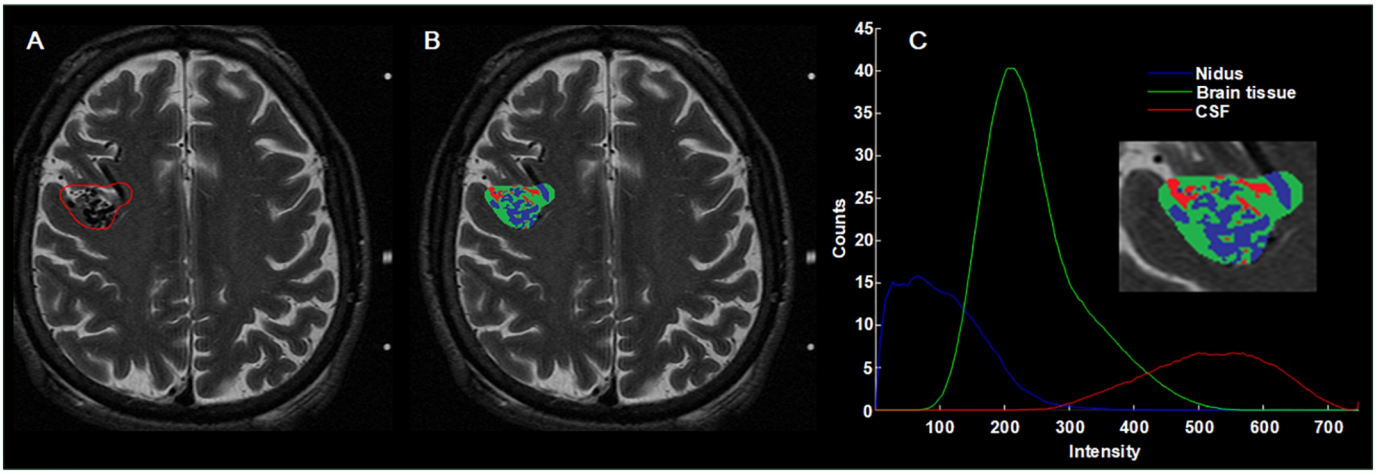

Fig. 1. Histographic characterization of cerebral AVM. The intensity histogram of the T2w image was obtained within the radiation exposure region, with the nidus (dark blue), brain tissue (green), and CSF (red) demarcated manually. (A) The red curve indicates the region exposed to radiation; (B) The blue, green, and red colors respectively indicate the nidus, brain tissue, and CSF delineated via manual segmentation. (C) Intensity histogram of nidus, brain tissue, and CSF obtained using manual segmentation within the region exposed to radiation.

This is achieved using fuzzy C-means clustering (Bezdek, 1981). This function is detailed below, with the information expressed as a value between 0 and 1, indicating the degree to which each voxel belongs to each cluster. The expected number of clusters is N, which is equal to 3 (nidus, brain tissue, and CSF). There are D voxels in the radiation exposure region of the T2w images (x_1,x_2, …x_D). Each voxel has its own grayscale value. For example, for data point x_i in a brain T2w image set, the sum of the membership grades belonging to the respective clusters is equal to 1. The function for fuzzy clustering is as follows:

$$\sum_{j=1}^{N=3} u_{ij} = 1,\ i = 1,\ 2,\ \ldots, D$$

The objective function is defined according to matrix U:

$$J_m = \sum_{i=1}^{D}\sum_{j=1}^{N=3} u_{ij}^{m}\ \|x_i - c_j\|^2$$

where m is the fuzzy partition matrix exponent that controls the degree of fuzzy overlap; c_j is the center of the jth cluster; and u_{ij} is the degree of membership of data point x_i in the jth cluster.

Fuzzy clustering is performed as follows:

Step 6.1. Cluster u_{ij} is randomly initialized.

Step 6.2. The centers of the various clusters (nidus, brain tissue, and CSF) are calculated as follows:

$$c_j = \frac{\sum_{i=1}^{D} u_{ij}^{m} x_i}{\sum_{i=1}^{D} u_{ij}^{m}}$$

Step 6.3. u_{ij} is renewed according to the following formula.

$$u_{ij} = \frac{1}{\sum_{k=1}^{N=3}\left(\frac{\|x_i - c_j\|}{\|x_i - c_k\|}\right)^{\frac{2}{m-1}}}$$

Step 6.4. The objective function J_m is calculated.

Step 6.5. Steps 2–4 are repeated iteratively until self-improvement J_m is smaller than a specified threshold or until a specific number of iterations has been performed. For example, the minimum improvement J_m could be set at 1e-5 and the maximum number of iterations could be set at 100.

Step 7. The volumes or percentages of the nidus, brain tissue, and CSF within the ROI are calculated.

2.5. Quantitative evaluation

Based on the Dice similarity index (SI) (Dice, 1945), sensitivity and specificity were calculated to determine the degree of conformity between automatic and manual segmentation in the GKRS plan of 25 patients with cerebral AVM. The agreement between the proposed algorithm and manual method in terms of volumetric measurement was evaluated using the intraclass correlation coefficient (ICC) (McGraw and Wong, 1996). Bland–Altman plots were used to assess systematic dissimilarity (Bland and Altman, 1999).

2.6. Clinical application

The automated clustering algorithm was used to analyze patients with unruptured cerebral AVM who were treated at Taipei Veterans General Hospital before 2012 and underwent follow-up for at least 3 years. A total of 40 patients were enrolled for clinical analysis. Our objective was to determine whether the volume of intervening brain parenchyma in the nidus of cerebral AVM is associated with increased ARE rates following GKRS.

3. Results

The ICCs in the delineation of the nidus, brain tissue, and CSF were 0.894, 0.882, and 0.714, respectively. Fig. 3 presents an example of the image analysis used in the clustering of the nidus, brain tissue, and CSF as well as the intensity distribution. The regions demarcated manually by the neurosurgeon are as follows: nidus (dark blue), brain tissue (green), and CSF (red). The regions demarcated by the algorithm are as follows: nidus (bright blue), brain tissue (green), and CSF (red). Linear regression analysis yielded the following regression coefficients and regression slopes for the three regions: nidus (R^2 = 0.873 and slope of 1.136), brain tissue (R^2 = 0.905 and slope of 0.778), and CSF (R^2 = 0.639 and slope of 0.781), as shown in Fig. 4A. The Bland-Altman plot in Fig. 4B indicates a slight overestimation of the nidus (bias of 0.286 ml) and CSF (bias of 0.242 ml) as well as a pronounced underestimation of brain tissue (bias of 0.528 ml). Clearly, the results obtained using automated clustering are strongly correlated with those obtained via manual clustering.

We also used SI to determine the degree to which the proposed automated segmentation method agrees with manual clustering in terms of sensitivity, specificity, and average performance for the three types of tissue. The proposed algorithm outperformed manual clustering (the gold

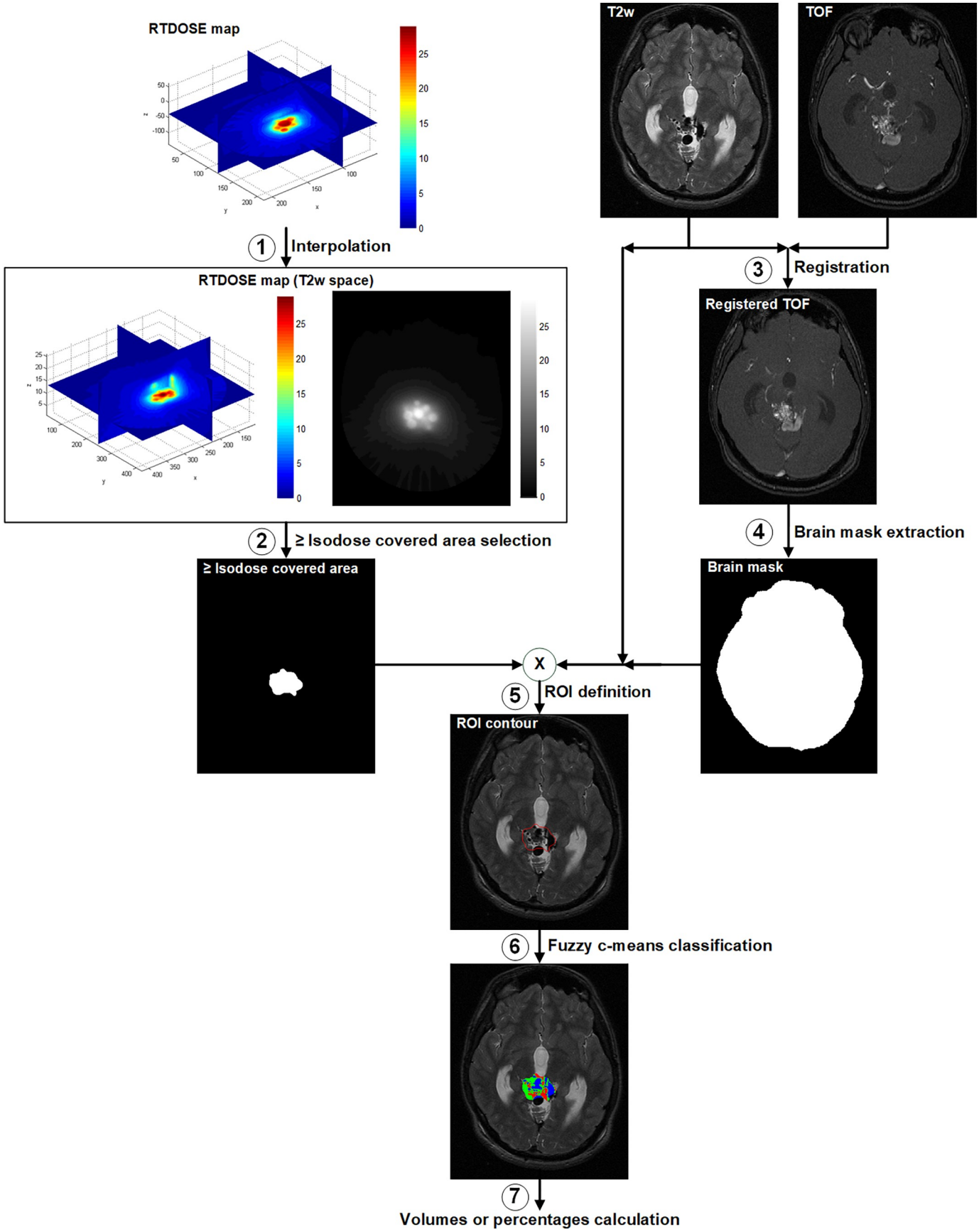

Fig. 2. Schematic diagram showing the workflow employed for image analysis and automated segmentation. The process includes seven steps: interpolation, selection of isodose coverage area, registration, brain mask extraction, ROI definition, Fuzzy c-means classification, and calculation of volumes or percentages of the various brain tissues.

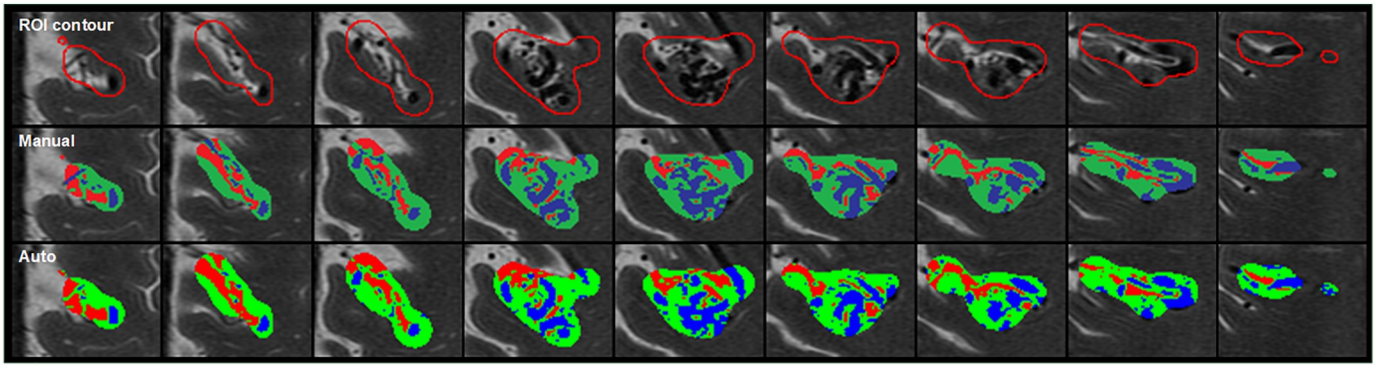

Fig. 3. Radiation exposure region, manual segmentation, and automated segmentation (top to bottom) in T2w images. The red curve indicates the boundary of the prescription isodose region. The blue, green, and red colors respectively indicate the nidus, brain tissue, and CSF.

standard) in terms of sensitivity and specificity in detecting the nidus: SI = (74.86 ± 1.30)% (mean ± standard deviation); sensitivity = (83.05 ± 11.91)%, and specificity = (86.73 ± 10.31)%. The results for brain tissue were as follows: SI = (79.50 ± 6.01)%; sensitivity = (73.05 ± 9.77)%; and specificity = (85.53 ± 7.13)%. The results for CSF were as follows: SI = (69.57 ± 15.26)%; sensitivity = (89.86 ± 5.87)%; and specificity = (92.36 ± 4.35)%. An SI value exceeding 0.7 is regarded as strong agreement (Bartko, 1991; Zijdenbos et al., 1994). Image analysis and automated segmentation required less than 1.523 ± 0.694 s to complete.

Table 1 lists the percentages of the three forms of brain tissue within the radiation exposure region as determined using automated clustering. Among the 25 patients, the lowest percentage of brain tissue was 37.13%, whereas the highest percentage of brain tissue was 70.85%, highlighting the high degree of variance that can be expected in the amount of brain tissue exposed to radiation during GKRS.

Finally, we correlated the results obtained using the imaging algorithm and clinical follow-up results from the other 40 AVM patients with unruptured AVM who underwent upfront GKRS only. This included 19 female and 21 male patients. The median age of these patients was 35 years old (range from 20 to 80 y/o). The median follow-up time was 71.5 months (range from 20 to 217 months). The median volume of the prescription isodose region was 21 ml (range from 7 to 53 ml). The median prescription peripheral dose for the nidus was 17Gy (range from 15 to 18.5Gy). We adopted the grading system proposed by Yen et al. (2013) to evaluate the severity of ARE. Briefly, Grade I AREs indicate slight changes in imaging that impose no mass effect on the surrounding brain tissue. Grade II AREs indicate moderate changes that cause effacement of the sulci or compression of the ventricles. Grade III AREs indicate severe changes that cause a midline shift of the brain. AREs were identified in 27 patients (17 patients with grade I, 9 patients with grade II and 1 patient with grade III), which was significantly related to the percentage of brain tissue within the prescription isodose range (53.3% vs. 44.6%, p = .001) in Fig. 6.

4. Discussion

4.1. The advantages of FCM over other methods

Prior to this study, we used artificial markers to label the nidus, brain tissue, and CSF within the ROI identified by neurosurgeons or radiologists. We then used the support vector machine supervised classifier for training and classification. Unfortunately, the analysis results obtained using a supervised classifier were highly biased by the contrast and brightness of individual images, which proved difficult to normalize between images from every patient. Thus, we opted for an unsupervised classifier to segment the various forms of brain tissue within the ROI and thereby avoid bias. The high SI of FCM clustering in this study can be attributed to the following features.

First, fuzzy clustering is based on the principle of assigning voxels to specific clusters according to the distribution characteristics observed in voxel intensity. The voxels within the ROI are classified using different algorithms. For example, voxels can be classified by setting

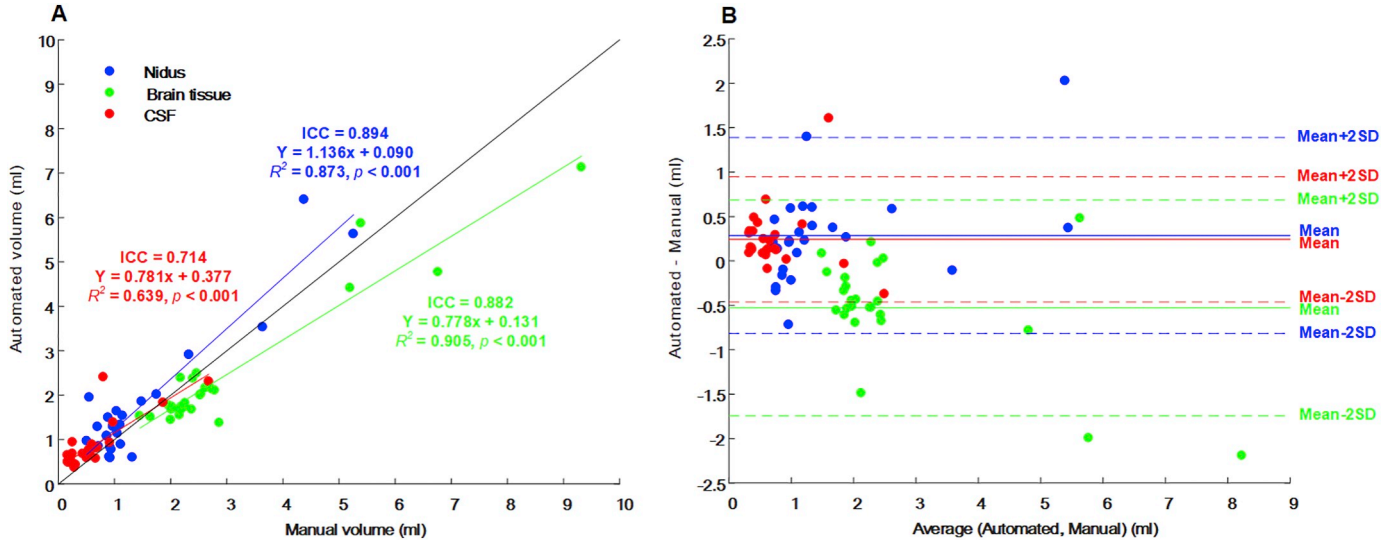

Fig. 4. Evaluation of nidus, brain tissue, and CSF segmentation results. (A) Linear regression (B) Bland-Altman plot. The red lines and dots represent the nidus; the green lines and dots represent brain tissue; and the blue lines and dots represent CSF.

Table 1
The percentages of the three tissues within the ROI under the prescription isodose radiation exposure by the proposed automatic clustering algorithm.

Patient	TP(Gy)	Volume	Nidus	BT	CSF	Location of AVM
1	18.5	3.00	26.19%	55.16%	18.66%	thalamus
2	18.5	3.78	32.68%	47.41%	19.91%	Hemisphere
3	19.5	4.38	45.07%	38.91%	16.02%	Hemisphere
4	18	11.43	48.40%	39.41%	12.19%	Hemisphere
5	16	11.71	29.48%	50.89%	19.63%	Brain stem
6	19	3.50	31.25%	48.73%	20.02%	Hemisphere
7	17.5	3.08	26.33%	57.12%	16.55%	Hemisphere
8	17	12.45	24.17%	56.55%	19.29%	Hemisphere
9	18	3.18	23.24%	48.31%	28.45%	Cerebellum
10	18	3.03	35.65%	47.36%	17.00%	Hemisphere
11	17	3.40	29.94%	52.11%	17.95%	Cerebellum
12	18.5	4.25	35.03%	48.14%	16.83%	Basal ganglia
13	18	4.02	19.27%	59.60%	21.13%	Hemisphere
14	20	4.04	25.88%	53.60%	20.52%	Cerebellum
15	18.5	4.24	34.65%	50.17%	15.18%	Basal ganglia
16	18.5	4.27	31.07%	51.51%	17.42%	Hemisphere
17	20	3.03	18.79%	60.29%	20.92%	Hemisphere
18	18	2.96	31.64%	53.20%	15.16%	Hemisphere
19	20	3.41	16.14%	70.85%	13.01%	Lateral ventricle
20	18.5	13.01	48.70%	37.13%	14.16%	Hemisphere
21	18.5	3.70	51.93%	37.13%	10.94%	Hemisphere
22	18.5	4.36	28.86%	48.87%	22.27%	Basal ganglia
23	17.8	3.93	42.05%	43.70%	14.25%	Hemisphere
24	18	3.23	26.00%	48.44%	25.56%	Brain stem
25	18.3	4.28	40.96%	49.21%	9.84%	Hemisphere
MEAN	18.32	5.03	32.13%	50.15%	17.71%	
STDEV	0.94	3.22	9.61%	7.68%	4.32%	

Note: BT = brain tissue, TP indicates margin dose.

intensity thresholds pertaining to each of the tissue types, or by using the unsupervised fuzzy clustering method. FCM is based on the principle of fuzzy clustering; however, each data point may belong to different clusters with different membership grades. In other words, no data point absolutely belongs to any cluster. Rather, each data point is represented as a number between 0 and 1, indicating the degree to which each data point belongs to each cluster. This makes it possible to examine the membership grades of each data point for all of the clusters in the membership grade matrix. The data point is then assigned to the cluster with the highest value.

Second, brain masks extracted from a registered TOF are more effective than those obtained from T2w images. The contrast assigned to the various types of tissue varies according to the type of image, which means that different types of MR images can be selected for the extraction of mask images. For example, Fig. 5A shows a T2w image in which the left black portion within the periphery of the brain is a cerebral AVM. Fig. 5B shows a brain mask image extracted from Fig. 5A, in which the brain region near the nidus is not within the region of the extracted mask. Fig. 5C shows a registered TOF image obtained from the TOF image registered to a T2w image of the same patient in which the nidus is displayed in brighter gray. Fig. 5D shows a brain mask image extracted from Fig. 5C, in which the extracted mask covers the brain region near the nidus. Fig. 5A and Fig. 5C are MR images obtained from the same patient; however, the brain mask images extracted from the two figures differ considerably in terms of range, as shown in Fig. 5B and Fig. 5D. This means that mask images must be extracted from an appropriate type of MR image based on the location of the target.

4.2. Using computers to calculate tissue components within the nidus margin of cerebral AVM

One previous study demonstrated that the radiation dose required to obliterate the AVM nidus is approximately 18–22 Gys (Flickinger et al., 1996). This dose is equal to the effective dose required to treat malignant brain tumors, and exceeds the tolerance of normal brain tissue. However, unlike GKRS treatment for solid, well-defined brain tumors, GKRS treatment for AVMs exposes a greater amount of normal brain parenchyma to risky high radiation doses due to the complex morphology of the AVM nidus. Determining the long-term effects of exposing brain parenchyma to radiation is problematic due to the lack of image analysis tools that are capable of objectively calculating the precise volume and percentage of brain tissue exposed to radiation during GKRS. Manual segmentation is time consuming and vulnerable to inter-reader variation, leaving physicians no choice but to estimate the risk of adverse radiation effects according to the brain tissue/nidus ratio.

Automating the clustering procedure makes it possible to quantify the ratios of the various types of tissue within the ROI quickly and easily. Several previous papers have described autosegmentation based on clustering using MR images to facilitate brain tumor detection (Sauwen et al., 2016; Emblem et al., 2009). However, to the best of our knowledge, our algorithm is the first automatic segmentation method that uses images of cerebral AVMs. Our results also appear to correlate with important clinical responses in patients undergoing GKRS for AVM.

4.3. Clinical importance of the proposed algorithm

Cerebral AVMs are a leading cause of intra-cerebral hemorrhaging in young adults (Al-Shahi and Warlow, 2001). The risk of re-bleeding in ruptured cerebral AVM is relatively high; therefore, a ruptured AVM requires more aggressive treatment. On the other hand, the risk of bleeding in unruptured AVMs has been reported at 2 to 4% (Ondra et al., 1990; Itoyama et al., 1989). Therefore, the management of unruptured cerebral AVMs is controversial. GKRS is less invasive than other treatment options and has the fewest acute side-effects. The most common complications after GKRS are the symptoms of ARE. Indeed, the incidence of ARE in follow-up images after GKRS is reported to be 30–60% (Flickinger et al., 1992; Ganz et al., 2009).

Several factors, including radiation dose and target volume, have been identified as important predictors of radiological outcomes. Other risk factors for ARE include prior hemorrhage (Hayhurst et al., 2012), AVM location (Flickinger et al., 1998), and repeated radiosurgery (Flickinger et al., 2002). Most AREs occur 1–24 months after GKS; however, they are generally transient and self-limited (Flickinger et al., 1997). Nonetheless, some AREs remain long after complete obliteration, resulting in a permanent complex lesion in the brain, which can cause severe symptoms over the long term. In 2005, Izawa etc. reported long-term complications in 9.3% of cases in their series (Izawa et al., 2005).

Two prospective randomized trials have reported significantly worse outcomes following intervention for unruptured cerebral AVMs (Mohr et al., 2014; Wedderburn et al., 2008). Treatment suggestions for AVMs, especially unruptured AVMs, have become increasingly conservative due to the fact that the complication rate after treatment may be higher than the natural bleeding rate of AVMs. We believe that the method of quantitatively analyzing the brain/nidus ratio proposed in this study could be highly beneficial to physicians seeking to optimize dosimetry. In other words, our proposed method should help to maximize therapeutic effects and minimize complications.

Our algorithm allows the various compositions of the AVM nidus delineated during the GKRS plan to be accurately identified. Furthermore, our findings demonstrate that a higher percentage of intervening brain parenchyma in the nidus of cerebral AVM is correlated with a higher prevalence of ARE following GKRS. Previous studies have reported on many other factors, such as overall AVM size, patient age, and prescribed radiation dose, which could confound the correlation with radiation injury after GK treatment (Joint Writing Group of the Technology Assessment Committee American Society of Interventional and Therapeutic Neuroradiology et al., 2001; Pan et al., 2000; Yen et al., 2013). Unfortunately, we would require a greater number of AVM patients if we were to discuss the correlation between these confounds. Our objective in this study was to emphasize the clinical importance of calculating the various tissue percentages within the prescription isodose radiation exposure region. The relationship between the various

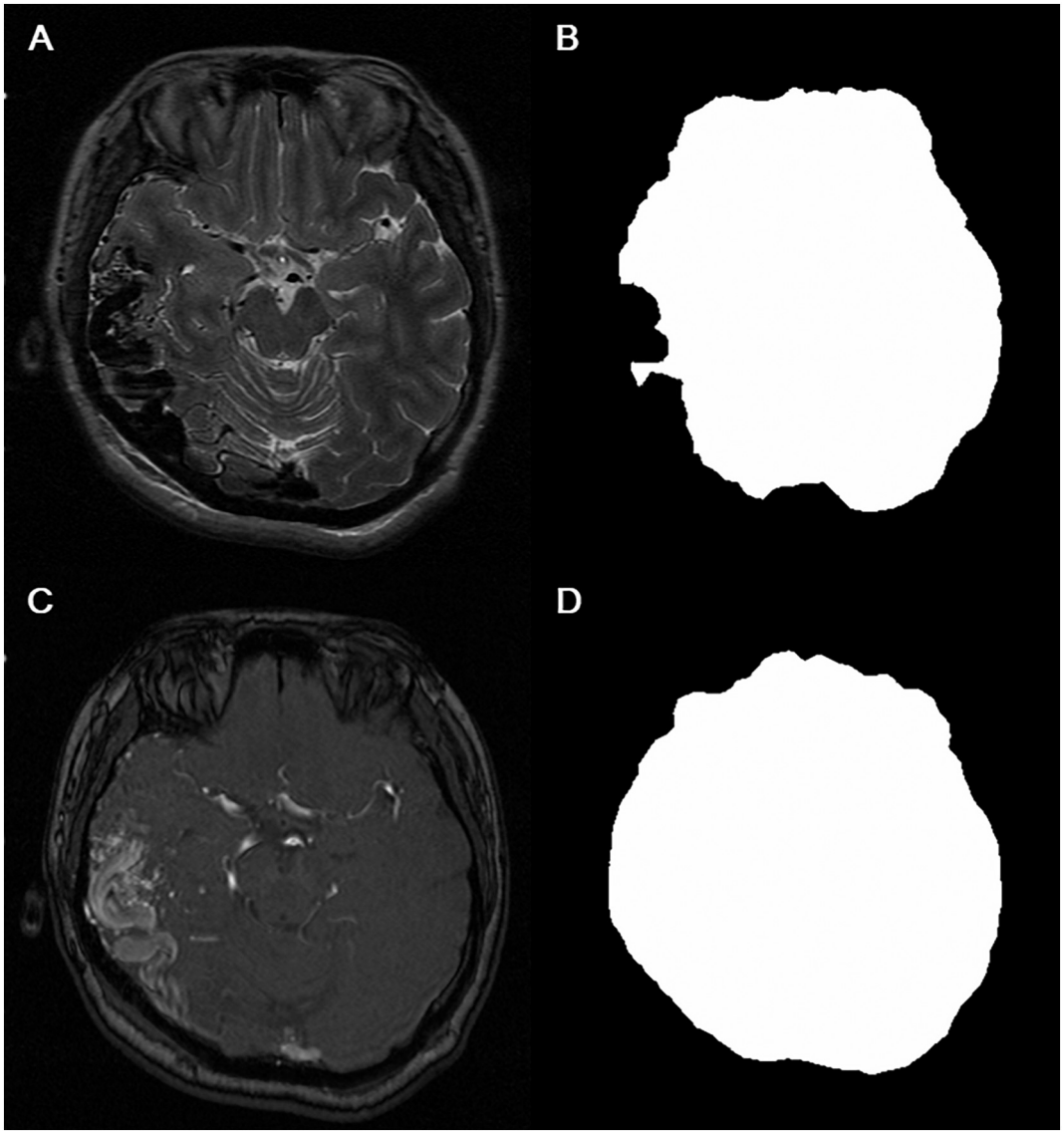

Fig. 5. Brain mask extraction. (A) T2w image, (B) brain mask image extracted from (A), (C) TOF image, (D) brain mask image extracted from (C) of patient with cerebral AVM. The brain mask that was extracted from the registered TOF was superior to the brain mask obtained from the T2w image when the AVM was located at the periphery of the brain.

confounds could be undertaken in the future using multiple medical centers to enroll a sufficient number of patients. Further clinical studies on the use of the proposed algorithm could help to elucidate the long-term effects of radiation on the brain and nidus. This means that the proposed algorithm could be a valuable tool for physicians making treatment decisions for AVM patients or formulating Gamma knife treatment plans.

4.4. Limitations of the study

Our initial objective was to validate the proposed methodology; therefore, we only enrolled a small number of patients. As a result, the study was susceptible to bias with regard to patient selection and treatment. The 1.5 T scanner is no longer considered a state-of–the-art device; however, in our hospital, FSE T2WI for GK treatment is always performed using a 1.5 T with birdcage head coil, 2D 3 mm slice thickness, and 0 mm slice gap. The 1.5 T scanner is preferred because imaging torsion caused by susceptibility artifacts from the stereotaxic frame is more prominent when using a 3.0 T scanner. Instead of a multi-channel head coil, we use a birdcage head coil (lacking accelerating ability) to accommodate the stereotaxic frame. The scanning time for 3D FSE T2WI using a birdcage head coil would be far too long.

We opted for relatively thin slices (3 mm) for 2D acquisition in order to strike a reasonable balance between SNR and scanning time. In the future, it would be interesting to verify our methodology using pre-GK 3D images acquired at higher spatial resolution on a state-of-the-art scanner.

A greater number of AVM cases and higher resolution images could improve the performance of the proposed methodology. In addition, our results are not necessarily applicable to cases of ruptured AVM or to cases involving other forms of treatment, such as surgery or embolization, prior to GKRS. Previous insult and bleeding may interfere with the autosegmentation process, potentially reducing the accuracy of segmentation results.

5. Conclusions

In this study, we developed a fully automated algorithm that uses unsupervised classification via fuzzy c-means clustering for the analysis of T2 weighted images of the Gamma knife plan. Our algorithm is able to calculate the percentages of the nidus, brain tissue, and CSF within the prescription isodose radiation exposure region. Analysis of the

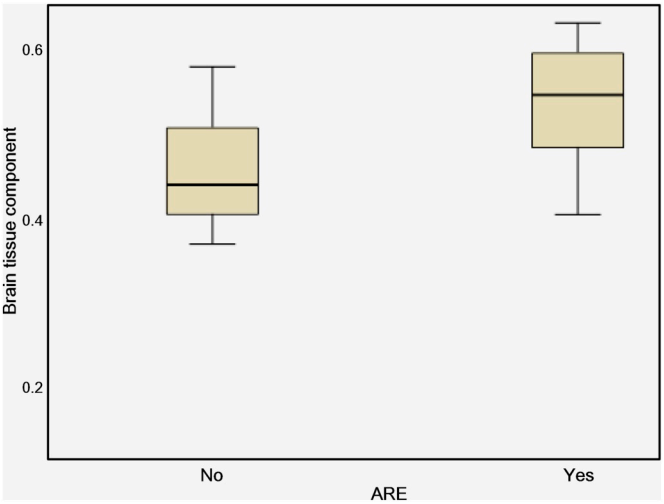

Fig. 6. Box plot showing the correlation between ARE and the brain tissue component of cerebral AVM. Cases with a greater number of brain tissue components are prone to ARE following radiosurgery ($p = .001$).

results yielded by this algorithm could help to differentiate among the various tissue responses to radiation and their relationship with AREs following GKRS.

Acknowledgments

This work was financially supported by the "Center for Neuromodulation Medical Electronics Systems" from The Featured Areas Research Center Program within the framework of the Higher Education Sprout Project by the Ministry of Education (MOE) in Taiwan and partly supported by the Ministry of Science and Technology (MOST) of Taiwan under Grant MOST 107-2221-E-009-103.

Conflicts of interest

None of the authors have any conflicts of interest to declare.

References

Al-Shahi, R., Warlow, C., 2001. A systematic review of the frequency and prognosis of arteriovenous malformations of the brain in adults. Brain 124, 1900–1926.
Al-Shahi, R., Bhattacharya, J.J., Currie, D.G., Papanastassiou, V., Ritchie, V., Roberts, R.C., Sellar, R.J., Warlow, C.P., Scottish Intracranial Vascular Malformation Study Collaborators, 2003. Scottish intracranial vascular malformation study (SIVMS): Evaluation of methods, ICD-10 coding, and potential sources of bias in a prospective, population-based cohort. Stroke 34, 1156–1162.
Bartko, J.J., 1991. Measurement and reliability: statistical thinking considerations. Schizophr. Bull. 17, 483–489.
Bezdek, James C., 1981. Pattern Recognition with Fuzzy Objective Function Algorithms. Plenum Press, New York.
Bland, J.M., Altman, D.G., 1999. Measuring agreement in method comparison studies. Stat. Methods Med. Res. 8, 135–160.
Bollet, M.A., Anxionnat, R., Buchheit, I., Bey, P., Cordebar, A., Jay, N., Desandes, E., Marchal, C., Lapeyre, M., Aletti, P., Picard, L., 2004. Efficacy and morbidity of arc-therapy radiosurgery for cerebral arteriovenous malformations: a comparison with the natural history. Int. J. Radiat. Oncol. Biol. Phys. 58, 1353–1363.
Cannon, R.L., Dave, J.V., Bezdek, J.C., 1986. Efficient implementation of the fuzzy c-means clustering algorithms. IEEE Trans. Pattern Anal. Mach. Intell. 8, 248–255.
Dice, L.R., 1945. Measures of the amount of ecologic association between species. Ecology 26, 297–302.
Emblem, K.E., Nedregaard, B., Hald, J.K., Nome, T., Due-Tonnessen, P., Bjornerud, A., 2009. Automatic glioma characterization from dynamic susceptibility contrast imaging: brain tumor segmentation using knowledge-based fuzzy clustering. J. Magn. Reson. Imaging 30, 1–10.
Flickinger, J.C., Lunsford, L.D., Kondziolka, D., Maitz, A.H., Epstein, A.H., Simons, S.R., Wu, A., 1992. Radiosurgery and brain tolerance: an analysis of neurodiagnostic imaging changes after gamma knife radiosurgery for arteriovenous malformations. Int. J. Radiat. Oncol. Biol. Phys. 23, 19–26.
Flickinger, J.C., Pollock, B.E., Kondziolka, D., Lunsford, L.D., 1996. A dose-response analysis of arteriovenous malformation obliteration after radiosurgery. Int. J. Radiat. Oncol. Biol. Phys. 36, 873–879.
Flickinger, J.C., Kondziolka, D., Pollock, B.E., Maitz, A.H., Lunsford, L.D., 1997. Complications from arteriovenous malformation radiosurgery: multivariate analysis and risk modeling. Int. J. Radiat. Oncol. Biol. Phys. 38, 485–490.
Flickinger, J.C., Kondziolka, D., Maitz, A.H., Lunsford, L.D., 1998. Analysis of neurological sequelae from radiosurgery of arteriovenous malformations: how location affects outcome. Int. J. Radiat. Oncol. Biol. Phys. 40, 273–278.
Flickinger, J.C., Kondziolka, D., Maitz, A.H., Lunsford, L.D., 2002. An analysis of the dose-response for arteriovenous malformation radiosurgery and other factors affecting obliteration. Radiother. Oncol. 63, 347–354.
Ganz, J.C., Reda, W.A., Abdelkarim, K., 2009. Adverse radiation effects after gamma knife surgery in relation to dose and volume. Acta Neurochir. 151, 9–19.
Gatos, I., Tsantis, S., Karamesini, M., Spiliopoulos, S., Karnabatidis, D., Hazle, J.D., Kagadis, G.C., 2017. Focal liver lesions segmentation and classification in nonenhanced T2-weighted MRI. Med. Phys. 44, 3695–3705.
Hathaway, R.J., Bezdek, J.C., 2001. Fuzzy c-means clustering of incomplete data. IEEE Trans. Syst. Man. Cybern. B. Cybern. 31, 735–744.
Hayhurst, C., Monsalves, E., van Prooijen, M., Cusimano, M., Tsao, M., Menard, C., Kulkarni, A.V., Schwartz, M., Zadeh, G., 2012. Pretreatment predictors of adverse radiation effects after radiosurgery for arteriovenous malformation. Int. J. Radiat. Oncol. Biol. Phys. 82, 803–808.
Itoyama, Y., Uemura, S., Ushio, Y., Kuratsu, J., Nonaka, N., Wada, H., Sano, Y., Fukumura, A., Yoshida, K., Yano, T., 1989. Natural course of unoperated intracranial arteriovenous malformations: study of 50 cases. J. Neurosurg. 71, 805–809.
Izawa, M., Hayashi, M., Chernov, M., Nakaya, K., Ochiai, T., Murata, N., Takasu, Y., Kubo, O., Hori, T., Takakura, K., 2005. Long-term complications after gamma knife surgery for arteriovenous malformations. J. Neurosurg. 102 (Suppl), 34–37.
Joint Writing Group of the Technology Assessment Committee American Society of Interventional and Therapeutic Neuroradiology, Joint Section on Cerebrovascular Neurosurgery a Section of the American Association of Neurological Surgeons and Congress of Neurological Surgeons, Section of Stroke and the Section of Interventional Neurology of the American Academy of Neurology, Atkinson, R.P., Awad, I.A., Batjer, H.H., Dowd, C.F., Furlan, A., Giannotta, S.L., Gomez, C.R., Gress, D., Hademenos, G., Halbach, V., Hemphill, J.C., Higashida, R.T., Hopkins, L.N., Horowitz, M.B., Johnston, S.C., Lawton, M.W., McDermott, M.W., Malek, A.M., Mohr, J.P., Qureshi, A.I., Riina, H., Smith, W.S., Pile-Spellman, J., Spetzler, R.F., Tomsick, T.A., Young, W.L., 2001. Reporting terminology for brain arteriovenous malformation clinical and radiographic features for use in clinical trials. Stroke 32, 1430–1442.
Lunsford, L.D., Kondziolka, D., Flickinger, J.C., Bissonette, D.J., Jungreis, C.A., Maitz, A.H., Horton, J.A., Coffey, R.J., 1991. Stereotactic radiosurgery for arteriovenous malformations of the brain. J. Neurosurg. 75, 512–524.
Maes, F., Collignon, A., Vandermeulen, D., Marchal, G., Suetens, P., 1997. Multimodality image registration by maximization of mutual information. IEEE Trans. Med. Imaging 16, 187–198.
McGraw, K.O., Wong, S.P., 1996. Forming inferences about some intraclass correlation coefficients. Psychol. Methods 1, 30–46.
Mohr, J.P., Parides, M.K., Stapf, C., Moquete, E., Moy, C.S., Overbey, J.R., Al-Shahi Salman, R., Vicaut, E., Young, W.L., Houdart, E., Cordonnier, C., Stefani, M.A., Hartmann, A., von Kummer, R., Biondi, A., Berkefeld, J., Klijn, C.J., Harkness, K., Libman, R., Barreau, X., Moskowitz, A.J., International ARUBA Investigators, 2014. Medical management with or without interventional therapy for unruptured brain arteriovenous malformations (ARUBA): a multicentre, non-blinded, randomised trial. Lancet 383, 614–621.
Ogilvy, C.S., Stieg, P.E., Awad, I., Brown Jr., R.D., Kondziolka, D., Rosenwasser, R., Young, W.L., Hademenos, G., Special Writing Group of the Stroke Council, American Stroke Association, 2001. AHA scientific statement: Recommendations for the management of intracranial arteriovenous malformations: a statement for healthcare professionals from a special writing group of the stroke council, American stroke association. Stroke 32, 1458–1471.
Ondra, S.L., Troupp, H., George, E.D., Schwab, K., 1990. The natural history of symptomatic arteriovenous malformations of the brain: a 24-year follow-up assessment. J. Neurosurg. 73, 387–391.
Pan, D.H., Guo, W.Y., Chung, W.Y., Shiau, C.Y., Chang, Y.C., Wang, L.W., 2000. Gamma knife radiosurgery as a single treatment modality for large cerebral arteriovenous malformations. J. Neurosurg. 93 (Suppl. 3), 113–119.
Sauwen, N., Acou, M., Van Cauter, S., Sima, D.M., Veraart, J., Maes, F., Himmelreich, U., Achten, E., Van Huffel, S., 2016. Comparison of unsupervised classification methods for brain tumor segmentation using multi-parametric MRI. Neuroimage Clin. 12, 753–764.
Smith, S.M., 2002. Fast robust automated brain extraction. Hum. Brain Mapp. 17, 143–155.
Wedderburn, C.J., van Beijnum, J., Bhattacharya, J.J., Counsell, C.E., Papanastassiou, V., Ritchie, V., Roberts, R.C., Sellar, R.J., Warlow, C.P., Al-Shahi Salman, R., Collaborators, S.I.V.M.S., 2008. Outcome after interventional or conservative management of unruptured brain arteriovenous malformations: a prospective, population-based cohort study. Lancet Neurol. 7, 223–230.
Yen, C.P., Matsumoto, J.A., Wintermark, M., Schwyzer, L., Evans, A.J., Jensen, M.E., Shaffrey, M.E., Sheehan, J.P., 2013. Radiation-induced imaging changes following gamma knife surgery for cerebral arteriovenous malformations. J. Neurosurg. 118, 63–73.
Zijdenbos, A.P., Dawant, B.M., Margolin, R.A., Palmer, A.C., 1994. Morphometric analysis of white matter lesions in MR images: Method and validation. IEEE Trans. Med. Imaging 13, 716–724.